PHYSICAL REVIEW B **105**, 195427 (2022)

Direct *d*-*d* hybridization mechanism for strong anisotropic carrier transport in layered Mo_2SBr_2

Haijun Liao,[1] Ye Xiao,[1,2] Yibin Yang,[1,2] Le Huang,[1,2,*] Huafeng Dong,[2,3] and Fugen Wu[1]
[1]*School of Materials and Energy, Guangdong University of Technology, Guangzhou 510006, China*
[2]*Guangdong Provincial Key Laboratory of Information Photonics Technology,*
Guangdong University of Technology, Guangzhou 510006, China
[3]*School of Physics and Optoelectronic Engineering, Guangdong University of Technology, Guangzhou 510006, China*

(Received 24 December 2021; revised 10 March 2022; accepted 11 May 2022; published 23 May 2022)

Transition metal sulfide halides such as Mo_2SBr_2 have exhibited excellent anisotropy in their electronic and optical properties. To explore the mechanism behind this strong anisotropic behavior, we performed first-principles calculations on the anisotropic mechanical, optical, and electronic properties of monolayer Mo_2SBr_2. We find that monolayer Mo_2SBr_2 demonstrates obvious anisotropy in its electron mobility, μ_e, with an extremely high μ_e of $10,356.08\,\mathrm{cm^2\,V^{-1}\,s^{-1}}$ along the *b* direction. We attributed this strong anisotropy in monolayer Mo_2SBr_2 to the unique characters in the orbital coupling. Our further studies show that direct *d*-*d* coupling between the nearest-neighboring Mo atoms plays a critical role in the unique carrier transport properties and strong anisotropy. Direct *d*-*d* coupling provides a fast hole transport channel along the *c* direction. Furthermore, wavefunction delocalization at the valence band maximum is significantly enhanced by this *d*-*d* hybridization, which further reduces the effective mass of holes. Our work provides physical insights into the origin of strong anisotropy in the photoelectric properties of transition metal sulfide halides. Transition metal sulfide halides are demonstrated to have great potential applications in novel nanoelectronic devices.

DOI: 10.1103/PhysRevB.105.195427

I. INTRODUCTION

Two-dimensional (2D) materials including graphene and transition metal dichalcogenides (TMDs) have attracted enormous attention due to their unique optoelectronic performance [1–3]. Meanwhile, the rapid development of novel optoelectronic devices and energy technologies has spawned a huge demand for special two-dimensional materials [4]. In view of nanoelectronic and photoelectric devices, high carrier mobility and conductivity of 2D materials are usually demanded for good performance. In contrast to 3D crystals, 2D materials usually hold great advantages in carrier mobility and conductivity due to the quantum confinement effect [5,6].

Recently, various 2D materials with high carrier mobility have been discovered to achieve outstanding photoelectric properties and excellent device performance. Graphene exhibited an ultrahigh mobility exceeding $10,000\,\mathrm{cm^2\,V^{-1}\,s^{-1}}$ at room temperature due to its linear energy dispersion [7]. Field effect transistors based on single-layer MoS_2 exhibited an electron mobility of $200\,\mathrm{cm^2\,V^{-1}\,s^{-1}}$ and a high on-off ratio of 10^8 [8]. Black phosphorus was reported to possess a moderate direct band gap and high hole mobility of $\sim 10,000\,\mathrm{cm^2\,V^{-1}\,s^{-1}}$ [9].

More recently, enormous efforts have been devoted to polarization-resolved detection in which linear dichroism is required for active materials. Many anisotropic 2D materials, such as bismuth oxyhalides and black phosphorus, have been explored in recent years [10–13]. Binary IV-VI chalcogenides with layered orthorhombic structures exhibit obvious anisotropy in their electronic and optical properties [14]. An *et al.* [15] reported an anisotropic electron mobility of 2D ZrB_2, endowing $ZrBr_2$ potential applications in negative differential conductance-based nanodevices. Furthermore, anisotropy of some 2D materials can be enhanced or induced by composition engineering, including alloying and anion/cation mutation. MoSSe exhibits anisotropy in carrier mobility, although the anisotropy value is still low, which restricts its applications in polarization-resolved detection [16].

So far, the high carrier mobility and high anisotropy in 2D materials mentioned earlier are attributed to the specific crystal symmetry and unique orbital coupling characters of band-edge states. Particularly, the ultrahigh mobility of graphene originates from the highly delocalized band-edge states formed by the big π coupling of C p_z orbitals [3,17]. Band-edge states of phosphorene are formed by the $3p$-$3p$ coupling between the nearest-neighboring P atoms. And the relative delocalization of P $3p$ orbitals combined with its covalent bonding characters endows phosphorene with high hole mobility [13]. Furthermore, obvious anisotropies in electronic, optical, and transport properties in phosphorene are induced by the distinct orbital coupling characters of band-edge states along the *b* and *c* directions [18]. Similarly, layered IV-VI semiconductors exhibit strong anisotropic photoelectric properties due to their structural anisotropy and direction-dependent orbital coupling [14].

As a derivative of TMDs, layered transition metal sulfide halides including Mo_2SBr_2 are also expected to have anisotropic photoelectric and transport properties due to their obvious structural anisotropies. Figure 1(a) gives

---

[*] huangle@gdut.edu.cn

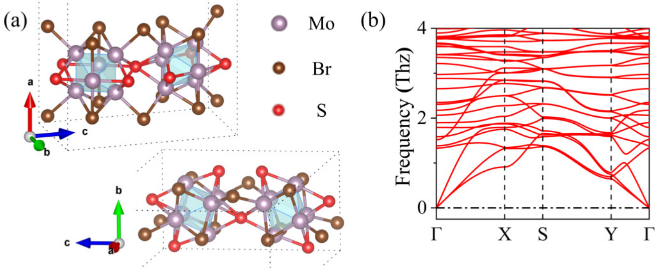

FIG. 1. (a) Three-dimensional views of the monolayer Mo_2SBr_2 structure. The direction of the vacuum layer is set as the *a* direction. (b) The phonon band structures of monolayer Mo_2SBr_2 along the high symmetric points in the Brillouin zone.

three-dimensional views of the crystal structure of monolayer Mo_2SBr_2. Monolayer Mo_2SBr_2 is derived from a Chevrel phase with [Mo_6] octahedron subunits covalently bonding in the *bc* plane and forming a layered structure along the *a* direction [19–21]. Along the *b*-axis, [Mo_6] octahedrons are directly bonded together with a corner-sharing pattern. Along the *c* direction, [Mo_6] octahedrons indirectly connect with two adjacent [Mo_6] through one S atom and two Br atoms. It should be mentioned that van der Waals (vdW) correction has little influence on the structural and electronic properties of monolayer Mo_2SBr_2, so vdW correction is not considered here.

Previous works have found that Mo_2SBr_2 exhibits obvious in-plane anisotropy in its electronic structure and photoelectric properties, which endows it with great application potential for polarized detection [22]. The mechanism of the anisotropy, however, is far from clear. What is more, because the Br atom is a little more electronegative and much larger in size than the S atom, the overlap of wavefunctions formed by Mo 4*d*-Br 4*p* coupling is reduced. According to the band coupling model [23], Mo_2SBr_2 is expected to have lower carrier mobility than MoS_2. Actually, Mo_2SBr_2 exhibits very good carrier transport performance in experiments [22], indicating an even higher carrier mobility than 2H-MoS_2. The origin of its high carrier mobility is also unknown.

Herein, theoretical calculations are performed to explore the physics of anisotropic properties of monolayer Mo_2SBr_2. Mechanical and electronic properties are investigated by using the density functional theory. It is demonstrated that the weak interlayer coupling exerts little influence on the physical properties of monolayer Mo_2SBr_2. The calculation of carrier mobility confirms the in-plane anisotropy of Mo_2SBr_2. Direct *d*-*d* orbital coupling between the nearest-neighboring Mo atoms is revealed to play a critical role in high carrier mobility. This direct *d*-*d* coupling that mainly occurs at the valence band maximum (VBM) facilitates hole transport along the *c* direction by providing a fast transport channel. Furthermore, the in-plane *d*-*d* orbital coupling of Mo atoms largely leads to anisotropy in the photoelectric and transport properties of Mo_2SBr_2.

II. COMPUTATIONAL METHODS

The Vienna Ab-initio Simulation Package (VASP) is the software package in which all the calculations of geometric structure optimization and electronic structure are performed [24]. The projector augmented wave potential is used to describe the pseudopotential in dealing with the interaction between the valence electron and the ionic substance. The exchange-correlation functional between electrons is described by the generalized-gradient approximation (GGA), with the exchange-correlation functional of Perdew-Burke-Ernzerhof (PBE) [25,26]. To overcome the band-gap underestimation of the GGA-PBE functional, the Heyd-Scuseria-Ernzerhof hybrid functional method (HSE06) with mixing 25% screened Hartree-Fock exchange to the GGA-PBE functional is used to obtain the accurate electronic structure [27]. The cutoff energy of the plane wave basis is set as 400 eV. The integration of the Brillouin zone uses the Gamma method to generate a $1 \times 6 \times 4$ k-point mesh. The force-convergence criterion for structural relaxation is 0.01 eV/Å on each atom. The thickness of the vacuum layer perpendicular to the two-dimensional plane is not less than 15 Å.

In order to explore detailed features of the chemical bonding in the employed system, crystal orbital Hamiltonian populations (COHPs) [28,29] of some related chemical bonding are calculated by using LOBSTER software. Projected COHP results can also be obtained from the chemical bonding analysis in LOBSTER. with reading and processing output data from VASP calculations [30,31].

To explore the transport properties of monolayer Mo_2SBr_2, lattice scattering (phonon scattering) and ionized impurity scattering are taken into consideration when calculating its carrier mobility [32,33]. In the low-energy range, coupling between carriers and the acoustic phonon coupling dominates the scattering, which can be calculated using the deformation potential theory proposed by Bardeen and Shockley [34]. Based on the effective mass approximation, the deformation potential theory can be well used to study the mobility of two-dimensional and one-dimensional materials [35].

Accordingly, carrier mobility of a 2D material is calculated as follows [36,37]:

$$\mu_{2D} = \frac{e\hbar^3 C_{2D}}{T k_B m_d m^* E_1^2}.$$

In the formula, e is the charge of the electron, ħ is the reduced Planck constant, and C_{2D} is the elastic modulus in the two-dimensional direction, which is defined as $C_{2D} = [\partial^2 E/\partial(\Delta l/l_0)^2]/S_0$ (where l_0 is the lattice constant in the transmission direction, Δl is the deformation in that direction, and S_0 is the plane area of the two-dimensional material), k_B is Boltzmann's constant, and T is temperature. During calculations, the temperature is taken as room temperature, 300 K. m^* is the effective mass of carriers in the transmission direction and $m_d = \sqrt{m_b^* \cdot m_c^*}$ is the average value of the effective mass of carriers. m_b^* and m_c^* are carrier effective masses along the b and c directions, respectively. E_1 is the deformation potential constant, which is the energy change of the conduction band minimum (CBM) or VBM under compressive or tensile strain. E_1 is defined as $E_1 = \Delta E_{VBM(CBM)}/(\Delta l/l_0)$. ΔE_{VBM} is the energy change of VBM for holes (CBM for electrons) induced by strains.

TABLE I. The band gap and formation energy of monolayer Mo_2SBr_2 and 2H-MoS_2 are calculated. Charge gains (ΔC) (in units of e) of each element from the Bader charge analysis are also listed.

Material	E_{g_HSE} (eV)	Formation energy (eV)	ΔC (Mo)	ΔC (S)	ΔC (Br)
2H-MoS_2	2.13	–2.760	–1.146	0.574	—
Mo_2SBr_2	1.85	–3.085	–0.863	0.824	0.451

III. RESULTS AND DISCUSSION

A. Geometric structure and lattice stability

Mo_2SBr_2 holds the space group of *Pmma*, with Mo_2SBr_2 layers stacking along the a direction. The optimized lattice constants of monolayer Mo_2SBr_2 are $b = 6.71$ Å and $c = 12.07$ Å. The optimized Mo-S bond length in monolayer Mo_2SBr_2 is 2.48 Å, which is a little longer than that of monolayer MoS_2 (2.42 Å).

To evaluate the structural stability of Mo_2SBr_2, formation energy, E_f, is calculated. The formation energy of Mo_2SBr_2 is defined as follows [38,39]:

$$E_f = \frac{E_{\text{total}}}{n_{\text{formula}}} - E(S) - 2(Mo) - 2E(Br),$$

where E_{total} in the formula represents the total energy of each Mo_2SBr_2 primitive cell; n_{formula} is the number of formula units in the primitive cell, which is 30 for Mo_2SBr_2; and $E(X)$ represents the average energy of each X atom in its elemental form.

The formation energy of 2H-MoS_2 is also calculated here for comparison. The calculated results of formation energy are shown in Table I. It is found that the formation energy of Mo_2SBr_2 is slightly lower than that of 2H-MoS_2, indicating good static stability of Mo_2SBr_2.

In order to check the dynamic stability of Mo_2SBr_2, the phonon spectrum is calculated and shown in Fig. 1(b) [40]. No imaginary frequency near the high-symmetry points demonstrates the dynamic stability of Mo_2SBr_2. Meanwhile, the highest frequency mode of the Mo_2SBr_2 monolayer reaches about 12 THz, suggesting the mechanical robustness of chemical bonding.

B. Electronic structure

In Fig. 2(a), the project band structure of monolayer Mo_2SBr_2 is calculated. HSE06 hybrid functional calculations are adopted to overcome the band-gap underestimation of GGA-PBE. It is found that Mo_2SBr_2 shows a direct band gap of 1.85 eV with both the VBM and CBM locating at the X(0.0 0.5 0.0) point. For comparison, the calculated band gap of monolayer 2H-MoS_2 is 2.13 eV, which is a little larger than that of Mo_2SBr_2. Furthermore, the VBM is mainly contributed by S p orbitals and the CBM mainly consists of Br p orbitals.

The diversity of bonding situations in the Mo_2SBr_2 crystal makes its electronic structure more complicated. To figure out the causes of the difference in the electronic structures of Mo_2SBr_2 and 2H-MoS_2, projected density of states (PDOS) of Mo_2SBr_2 is calculated in Fig. 2(b). It is found from Fig. 2(b) that both the VBM and CBM mainly consist of Mo d, S p, and Br p orbitals. Deeper bonding information can be further seen through the crystal orbital Hamiltonian population theory. The COHP of the Mo_2SBr_2 monolayer reveals that both band edges exhibit antibonding characters between the Mo d and anion p orbitals. Specifically, there are antibonding orbitals of the Mo-S bond and the Mo-Br bond on both the valence and conduction bands. The antibonding orbital of the Mo-S bond along the c direction is stronger than that of the Mo-Br bond mainly along the b direction.

Compared with 2H-MoS_2, Mo atoms in Mo_2SBr_2 have a different chemical environment, as shown in Fig. 3(a). Along the b direction, Mo_2SBr_2 is divided into five atomic layers. Mo(1), located in the innermost layer, coordinates to three S atoms along the c direction and two Br atoms along the a direction. Mo(2), located in the secondary outer layer, is adjacent to one S atom and three Br atoms. According to ligand field theory [41], a different crystal field-splitting model of Mo-d should occur in Mo_2SBr_2, as shown in Fig. 3(b) and (c). Detailed analysis based on crystal field theory reveals that d orbitals of Mo(1) split into one-fold d_{z^2}, two-fold d_{xz} and d_{yz}, one-fold $d_{x^2-y^2}$, and one-fold d_{xy}. And d orbitals of Mo(2) split into two-fold d_{xy} and d_{xz}, two-fold d_{yz} and d_{z^2}, and one-fold $d_{x^2-y^2}$.

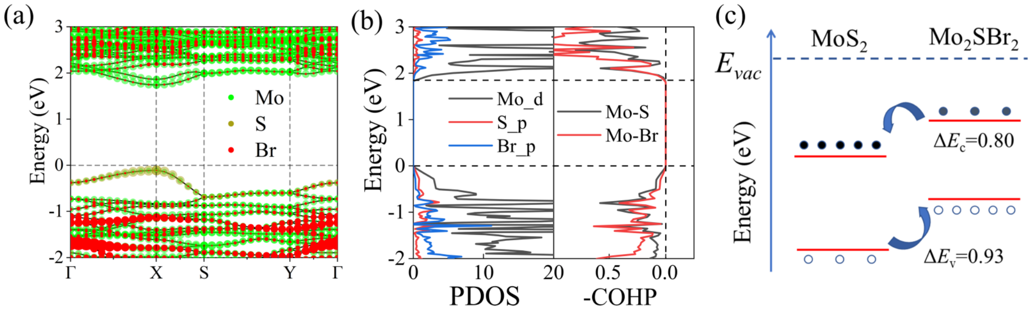

FIG. 2. (a) Projected band structure of monolayer Mo_2SBr_2. (b) Project density of states (PDOS) and crystal orbital Hamiltonian population (COHP) of Mo_2SBr_2. The VBM is taken as the energy reference. (c) The band alignment of 2H-MoS_2 and Mo_2SBr_2.

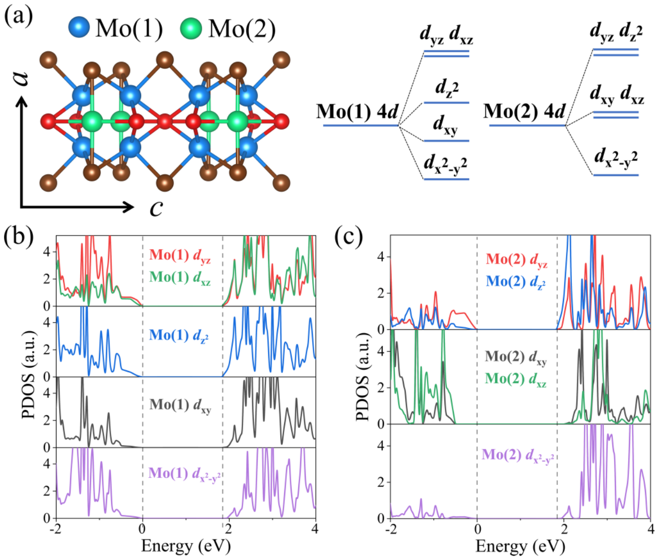

FIG. 3. (a) Crystal structure of Mo_2SBr_2 with Mo(1) and Mo(2) plotted in different colors. Crystal field splitting of 4d orbitals of Mo(1) and Mo(2) are also shown. Views (b) and (c) give the PDOS on Mo(1) and Mo(2), respectively.

In the orbital coupling model of Mo_2SBr_2, it is found that the VBM is mainly formed by antibonding states between Mo(1) d_{yz} and S p orbitals. And the CBM mainly originates from the antibonding between Mo(1, 2) d_{z^2}, d_{xz}, and Br p orbitals. Furthermore, Mo-S bonds are mainly formed along the c direction, while Mo-Br bonds are in-plane bonding. Consequently, the VBM that formed by Mo-S bonding has strong dispersion along the c direction and weak dispersion along the b direction, which is consistent with the results of band structures in Fig. 2(a). To evaluate the energy dispersion of the VBM and CBM, the band decomposed charge density at the X point is calculated in Fig. 4(a). It can be seen that the distributions of the band decomposed charge density of the VBM and CBM mainly localize on the Mo-S and Mo-Br bonds, respectively. Specifically, the band of the CBM that comes from Mo-Br antibonding states exhibits similar dispersion along the c and b directions. This direction-dependent dispersion of band edges leads to anisotropic characters in the electronic, optical, and carrier transport properties of Mo_2SBr_2. It is noted that a direct d-d coupling of Mo atoms is found in band-edge regions, which should have a significant impact on the electronic structure. To figure out the effect of this direct d-d coupling on the photoelectric and transport properties, the projected COHP of this d-d coupling is calculated in Fig. 4(b). It is found that this d-d coupling mainly comes from the d_{yz}-d_{yz} coupling. Combined with the Mo-S bonding at the VBM, the d-d orbital coupling further enhances the in-plane stiffness along the c direction of Mo_2SBr_2. Different from the VBM, direct d-d orbital coupling is absent at the CBM. The wavefunction of the CBM state is mainly derived from the coupling between the Br 4p_z and Mo d_{z^2} orbitals.

Further insights can be obtained by Bader charge analysis [42]. The average charge of each element in Mo_2SBr_2 is given in Table I. It is revealed that both the Mo-S and Mo-Br bonds have ionic and covalent properties. Comparing Bader charge results in 2H-MoS_2 (Table I), a little more charge exchange between the Mo and S atoms is found in Mo_2SBr_2, indicating stronger Mo-S bonding in Mo_2SBr_2. Further evidence comes from the shorter Mo-S bonds in Mo_2SBr_2. The stronger Mo-S bonding in Mo_2SBr_2 pushes its VBM higher than that in 2H-MoS_2. The band alignments of monolayer Mo_2SBr_2 and MoS_2 can provide further insight into this direct d-d coupling on electronic structures of Mo_2SBr_2. On one hand, this direct d-d coupling pushes the VBM and CBM of monolayer Mo_2SBr_2 upward. Especially for the VBM, stronger d-d coupling results in a larger shift-up in its energy position ($\Delta E_v = 0.93$eV) compared with that of the CBM ($\Delta E_c = 0.80$eV). As a result, the VBM and CBM of monolayer Mo_2SBr_2 are a little higher than those of monolayer MoS_2. On the other hand, compared with 2H-MoS_2, the direct d-d coupling in Mo_2SBr_2 gives rise to the enhanced delocalization of the band-edge states, which should result in smaller carrier effective masses and mobilities. As can be seen from the band alignment of Mo_2SBr_2/2H-MoS_2 in Fig. 2(c), Mo_2SBr_2/2H-MoS_2 tends to form a type II band alignment.

C. Mechanical properties

Previous works proved a strong correlation between polarization-resolved detection and anisotropic mechanical properties of semiconductors. For monolayer Mo_2SBr_2, the relationship between the elastic constant and the stiffness

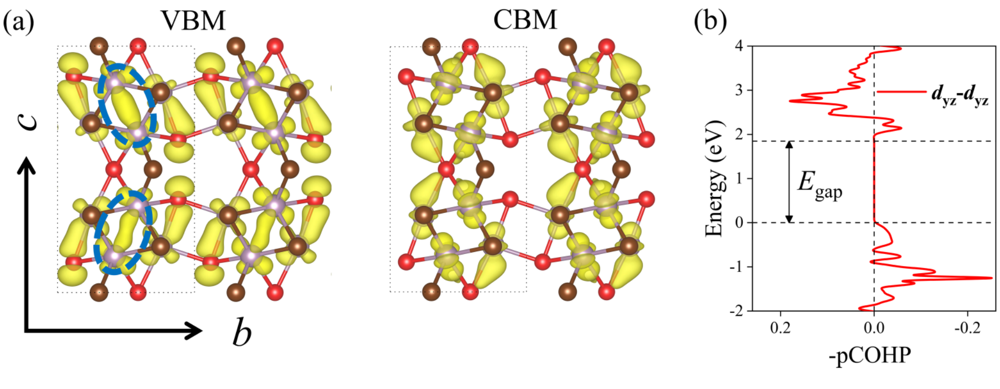

FIG. 4. (a) The distribution of band decomposed charge density of the CBM and VBM states. The isosurface value is set as 0.002 e Å^{-3}. (b) The projected COHP on the orbital coupling Mo d_{yz} and Mo d_{yz}.

TABLE II. Calculated minimum and maximum of in-plane elastic stiffness constants, Young's modulus Y (N/m), shear modulus G (N/m), and Poisson's ratio ν on the PBE functional level.

	Y (N/m)		G (N/m)		ν	
Material	Min	Max	Min	Max	Min	Max
2H-MoS_2	124.57	124.72	49.96	50.02	0.25	0.25
Mo_2SBr_2	50.62	90.70	16.84	39.16	0.13	0.50

modulus can be given according to Hooke's law:

$$\sigma_{\mathrm{ij}}=C_{ijkl}\cdot\varepsilon_{kl},$$

where σ_{ij} is the second-order Cauchy stress tensor, ϵ_{kl} is the second-order strain tensor, and C_{ijkl} is the fourth-order anisotropic stiffness coefficient. The number of independent elastic constants depends on the symmetry of the crystal [43]. For 2D Mo_2SBr_2, five nonzero C_{ijkl} should appear in matrix C. And nondiagonal elements should have relationship $C_{12}=C_{21}$. Thus, there are in matrix C [44],

$$C=\begin{bmatrix} C_{11} & C_{12} & 0 \\ C_{12} & C_{22} & 0 \\ 0 & 0 & C_{44} \end{bmatrix}.$$

The mechanical stability of a crystal lattice can be determined by the following criterions: $C_{11}>0\&C_{22}>0\&C_{44}>0\&C_{11}\cdot C_{22}>C_{12}^2$ [45]. The calculated elastic stiffness coefficients of 2H-MoS_2 and Mo_2SBr_2 are given in Table II.

Our results are in good agreement with previous work [8]. It is revealed that all the criteria for mechanical stability are satisfied for 2H-MoS_2 and Mo_2SBr_2. Table II also lists the minimum and maximum of Young's modulus [$Y(\theta)$], Poisson's ratio [$\nu(\theta)$], and the shear modulus [$G(\theta)$] of Mo_2SBr_2 [43,46]. Figure 5 shows the orientation-dependent mechanical quantities including Young's modulus [$Y(\theta)$], Poisson's ratio [$\nu(\theta)$], and the shear modulus [$G(\theta)$] of monolayer Mo_2SBr_2. It is found that $Y(\theta)$, $\nu(\theta)$, and $G(\theta)$ show strong dependence on the azimuth angle, indicating strong anisotropy of mechanical properties of monolayer Mo_2SBr_2. Specifically, monolayer Mo_2SBr_2 has higher Young's modulus $Y(\theta)$ and shear modulus $G(\theta)$ than 2H-MoS_2. This can be attributed to the shorter Mo-S bonds in Mo_2SBr_2 due to the intralayer *d*-*d* coupling. Moreover, the anisotropy in $Y(\theta)$ (90.70 N/m in the c direction vs. 86.55 in the b direction) of Mo_2SBr_2 is further enhanced by the direct *d*-*d* coupling.

D. Carrier mobility

Carrier mobility plays a critical role in device performance of photodetectors [47–50]. In order to investigate the potential capacity of Mo_2SBr_2 as active material for optoelectronic devices, carrier mobility was calculated by using the deformation potential theory. It can be concluded that the carrier mobility depends on three factors: the deformation potential E_1, carrier effective mass m^*, and the elastic modulus $C_{2\mathrm{D}}$ along the propagation direction. The carrier mobilities at room-temperature (300-K) 2H-MoS_2 and Mo_2SBr_2 in the b and c directions are calculated and summarized in Table III.

From Table III, we can find that the electron mobilities of 2H-MoS_2 in the b and c directions are 178.93 $\mathrm{cm^2\,V^{-1}\,s^{-1}}$ and 164.90 $\mathrm{cm^2\,V^{-1}\,s^{-1}}$, respectively. And the hole mobilities are 562.44 $\mathrm{cm^2\,V^{-1}\,s^{-1}}$ and 542.80 $\mathrm{cm^2\,V^{-1}\,s^{-1}}$, respectively. 2H-$MoS_2$ shows isotropic carrier mobility, which restricts its application in polarization-dependent optoelectronics. Unlike 2H-MoS_2, Mo_2SBr_2 exhibits obvious anisotropy in its carrier mobilities. The electron mobility along the b direction (10 356.08 $\mathrm{cm^2\,V^{-1}\,s^{-1}}$) is much larger than that of mobility along the c direction (914.21 $\mathrm{cm^2\,V^{-1}\,s^{-1}}$). The hole mobility along the b direction (211.81 $\mathrm{cm^2\,V^{-1}\,s^{-1}}$) is much smaller than that of mobility along the c direction (1122.18 $\mathrm{cm^2\,V^{-1}\,s^{-1}}$). Accordingly, the anisotropic degree of carrier mobility of the Mo_2SBr_2 monolayer is calculated as $\eta=\mu_b/\mu_c$. Large divergence of η from unit suggests strong anisotropy.

The anisotropic degree of carrier mobility of Mo_2SBr_2 is 11.33 for electrons and 0.19 for holes. This strong anisotropy in carrier mobility in Mo_2SBr_2 is attributed to the distinct deformation potential constant and the effective mass of carriers. Furthermore, the distribution of the band decomposed charge density of the CBM in Fig. 4(a) shows a much more delocalization feature along the c direction than that along the b direction, which results in a higher deformation potential constant along the c direction. A large deformation potential for electron transport along the c direction is caused. Moreover, due to the small distance (2.70 Å) between two Mo(2) atoms in [Mo_6] octahedron, the wavefunction of the VBM shows an obvious *d*-*d* orbital coupling of Mo(2)-Mo(2) along the c direction, which leads to a higher deformation potential for holes along the c direction, while the CBM shows no *d*-*d* coupling along the c direction. Although *d*-*d* coupling induces a higher deformation potential, a smaller effective mass will also be induced due to *d*-*d* coupling between Mo atoms. The *d*-*d* coupling will open a carrier transport channel,

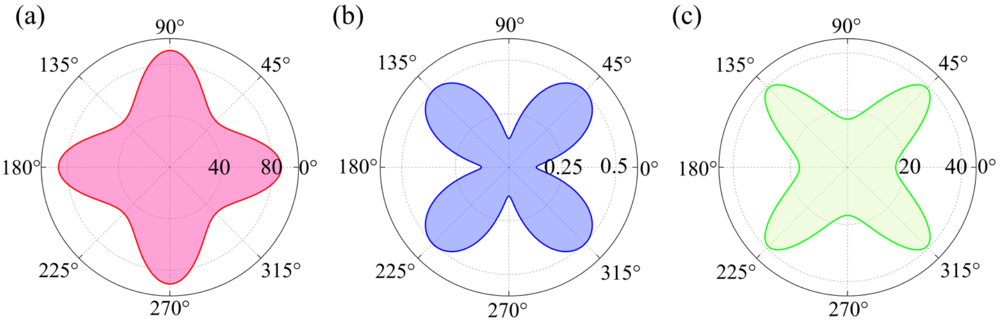

FIG. 5. Calculated orientation-dependent (a) Young's modulus $Y(\theta)$, (b) Poisson's ratio $\nu(\theta)$, and (c) shear modulus $G(\theta)$ of Mo_2SBr_2.

TABLE III. Calculated carrier effective masses m^*, deformation potential E_1 (eV), in-plane stiffness C_{2D} (N/m), and mobility μ (cm^2 V^{-1} s^{-1}) for electron e and hole h along the b and c directions in 2H-MoS$_2$ and Mo$_2$SBr$_2$. The temperature is set as room temperature (300 K).

Carrier type	Material	m_b^*/m_0	m_c^*/m_0	E_{1-b}	E_{1-c}	C_{2D-b}	C_{2D-c}	μ_b	μ_c
Electron	2H-MoS$_2$	0.46	0.48	7.63	7.98	116.84	128.70	178.93	164.90
	Mo$_2$SBr$_2$	0.79	0.92	0.48	2.25	85.31	92.53	10 356.08	914.21
Hole	2H-MoS$_2$	0.59	0.62	3.80	3.87	116.84	128.70	562.44	542.80
	Mo$_2$SBr$_2$	1.19	0.23	2.72	4.07	85.31	92.53	211.81	1122.18

which is a benefit to carrier mobility. As a result, hole mobility along the c direction, μ_c, is much larger than μ_b. Additionally, the *d*-*d* orbital coupling of Mo atoms in Mo$_2$SBr$_2$ results in larger electron mobility than 2H-MoS$_2$. Consequently, *d*-*d* orbital coupling of Mo atoms has a critical influence on the anisotropy of carrier mobility. This also coincides with the previous analysis: Mo$_2$SBr$_2$ has anisotropy in carrier mobility.

IV. CONCLUSION

In summary, first-principles calculations were performed to explore the structural, electronic properties of Mo$_2$SBr$_2$, with a focus on the anisotropy in these physical properties. Monolayer Mo$_2$SBr$_2$ has a direct band gap of 1.85 eV. Strong anisotropies in its mechanical and electronic properties were revealed. It is found that monolayer Mo$_2$SBr$_2$ demonstrates obvious anisotropy in its electron mobility, μ_e, with an extremely high μ_e of 10 356.08 cm^2 V^{-1} s^{-1} along the *b* direction. This strong anisotropy is attributed to the unique characters in the orbital coupling. Our further studies show that direct *d*-*d* coupling between the nearest-neighboring Mo atoms plays a critical role in the unique carrier transport properties and strong anisotropy. Direct *d*-*d* coupling provides a fast hole transport channel along the *c* direction. Furthermore, wavefuntion delocalization at the valence band maximum is enhanced by the direct *d*-*d* hybridization, which further reduces the effective mass of holes. All these results provide a deep understanding of the origin of strong anisotropy in the photoelectric properties of transition metal sulfide halides.

ACKNOWLEDGMENTS

This work was supported by the Science and Technology Program of Guangzhou (Grants No. 202102020389 and No. 202103030001), the National Natural Science Foundation of China (Grants No. 11804058 and No. 12064027), the Fund of Guangdong Provincial Key Laboratory of Information Photonics Technology (Grant No. 2020B121201011), and the Special Fund of Nanchang Hangkong University Graduate (Grant No. YC2020073). We also thank the Center of Campus Network & Modern Educational Technology, Guangdong University of Technology, Guangdong, China, for providing computational resources and technical support for this work.

---

[1] K. S. Novoselov, A. K. Geim, S. V. Morozov, D. Jiang, Y. Zhang, S. V. Dubonos, I. V. Grigorieva, and A. A. Firsov, Science **306**, 666 (2004).

[2] K. S. Novoselov, D. Jiang, F. Schedin, T. J. Booth, V. V. Khotkevich, S. V. Morozov, and A. K. Geim, Proc. Natl. Acad. Sci. USA **102**, 10451 (2005).

[3] A. Patra, M. A. More, D. J. Late, and C. S. Rout, J. Mater. Chem. C **9**, 11059 (2021).

[4] M. Z. Qin *et al.*, Adv. Colloid Inter. Sci. **297**, 102540 (2021).

[5] K. S. Novoselov, A. Mishchenko, A. Carvalho, and A. H. Castro Neto, Science **353**, aac9439 (2016).

[6] M. Liu, T. Liao, Z. Sun, Y. Gu, and L. Kou, Phys. Chem. Chem. Phys. **23**, 21376 (2021).

[7] Z. Zhuo, X. Wu, and J. Yang, Nanoscale **12**, 19359 (2020).

[8] K. F. Mak, C. Lee, J. Hone, J. Shan, and T. F. Heinz, Phys. Rev. Lett. **105**, 136805 (2010).

[9] H. Liu, Y. Du, Y. Deng, and P. D. Ye, Chem. Soc. Rev. **44**, 2732 (2015).

[10] J. Li, Y. Yu, and L. Zhang, Nanoscale **6**, 8473 (2014).

[11] J. Xiong, P. Song, J. Di, H. Li, and Z. Liu, J. Mater. Chem. A **7**, 25203 (2019).

[12] W. Liu, H. Bao, Y. Li, and F. Ma, Phys. Chem. Chem. Phys. **23**, 7080 (2021).

[13] H. Liu, A. T. Neal, Z. Zhu, Z. Luo, X. Xu, D. Tomanek, and P. D. Ye, ACS Nano **8**, 4033 (2014).

[14] G. Qin, Z. Qin, W. Z. Fang, L. C. Zhang, S. Y. Yue, Q. B. Yan, M. Hu, and G. Su, Nanoscale **8**, 11306 (2016).

[15] Y. An, J. Jiao, Y. Hou, H. Wang, R. Wu, C. Liu, X. Chen, T. Wang, and K. Wang, J. Phys. Condens. Matter **31**, 065301 (2019).

[16] L. Fu, X. Wang, and W. Mi, Appl. Surf. Sci. **566** 150683 (2021).

[17] A. H. Castro Neto, F. Guinea, N. M. R. Peres, K. S. Novoselov, and A. K. Geim, Rev. Mod. Phys. **81**, 109 (2009).

[18] M. Ezawa, J. Phys. Conf. Ser. **603**, 012006 (2015).

[19] C. Perrin, M. Potel, and M. Sergent, Acta Crystallogr. C Cryst. Struct. Commun. **39**, 415 (1983).

[20] R. Chevrel, M. Sergent, and J. Prigent, Mater. Res. Bull. **9**, 1487 (1974).

[21] V. E. Fedorov, A. V. Mishchenko, and V. P. Fedin, Russ. Chem. Rev. **54**, 408 (1985).

[22] X. J. Zhong *et al.*, Adv. Funct. Mater. **29**, 1902951 (2019).

[23] W. A. Harrison, *Elementary Electronic Structure. Revised edition* (World Scientific Publishing, Singapore, 2004).
[24] G. Kresse and J. Furthmuller, Phys. Rev. B **54**, 11169 (1996).
[25] J. P. Perdew, K. Burke, and M. Ernzerhof, Phys. Rev. Lett. **77**, 3865 (1996).
[26] J. P. Perdew, K. Burke, and Y. Wang, Phys. Rev. B **54**, 16533 (1996).
[27] M. Gajdos, K. Hummer, G. Kresse, J. Furthmuller, and F. Bechstedt, Phys. Rev. B **73**, 045112 (2006).
[28] R. Dronskowski and P. E. Bloechl, J. Phys. Chem. **97**, 8617 (2002).
[29] V. L. Deringer, A. L. Tchougreeff, and R. Dronskowski, J. Phys. Chem. A **115**, 5461 (2011).
[30] S. Maintz, V. L. Deringer, A. L. Tchougreeff, and R. Dronskowski, J. Comput. Chem. **37**, 1030 (2016).
[31] G. Tang, P. Ghosez, and J. Hong, J. Phys. Chem. Lett. **12**, 4227 (2021).
[32] K. Kaasbjerg, K. S. Thygesen, and K. W. Jacobsen, Phys. Rev. B **85**, 115317 (2012).
[33] K. Kaasbjerg, K. S. Thygesen, and A.-P. Jauho, Phys. Rev. B **87**, 235312 (2013).
[34] J. Bardeen and W. Shockley, Phys. Rev. **80**, 72 (1950).
[35] Y. Xu, J. Dai, and X. C. Zeng, J. Phys. Chem. Lett. **7**, 302 (2016).
[36] J. Qiao, X. Kong, Z. X. Hu, F. Yang, and W. Ji, Nat. Commun. **5**, 4475 (2014).
[37] C. X. Xia, J. Du, X. W. Huang, W. B. Xiao, W. Q. Xiong, T. X. Wang, Z. M. Wei, Y. Jia, J. H. Shi, and J. B. Li, Phys. Rev. B **97**, 115416 (2018).
[38] H. M. Tang, A.-A. Sun, and S.-P. Gao, Phys. Rev. Mater. **4**, 084004 (2020).
[39] J. T. Paul *et al.*, J. Phys. Condens. Matter **29**, 473001 (2017).
[40] O. I. Malyi, K. V. Sopiha, and C. Persson, ACS Appl. Mater. Interfaces **11**, 24876 (2019).
[41] E. Sacher, Phys. Rev. B **34**, 5130 (1986).
[42] M. Yu and D. R. Trinkle, J. Chem. Phys. **134**, 064111 (2011).
[43] V. Wang, Y.-Y. Liang, Y. Kawazoe, and W.-T. Geng, arXiv:1806.04285.
[44] M. Maździarz, 2D Mater. **6**, 048001 (2019).
[45] F. Mouhat and F. X. Coudert, Phys. Rev. B **90**, 224104 (2014).
[46] V. Wang, N. Xu, J. C. Liu, G. Tang, and W. T. Geng, Comput. Phys. Commun. **267**, 108033 (2021).
[47] M. V. Fischetti and S. E. Laux, J. Appl. Phys. **80**, 2234 (1996).
[48] H. Li, Q. Zhang, P. Shi, Y. Wu, and X. Zhang, Opt. Eng. **60**, 082008 (2020).
[49] T. Yu, Z. Zhao, Y. Sun, A. Bergara, J. Lin, S. Zhang, H. Xu, L. Zhang, G. Yang, and Y. Liu, J. Am. Chem. Soc. **141**, 1599 (2019).
[50] C. Liu, X. Liu, G. Zheng, X. Gong, C. Yang, H. Liu, L. Zhang, C. L. Anderson, B. He, L. Xie, R. Zheng, H. Liang, Q. Zhou, Z. Zhang, J. Chen, and Y. Liu, J. Mater. Chem. A **9**, 23497 (2021).